PHYSICAL REVIEW B **101**, 214102 (2020)

Antichiral one-way edge states in a gyromagnetic photonic crystal

Jianfeng Chen,[*] Wenyao Liang,[*] and Zhi-Yuan Li[†]
School of Physics and Optoelectronics, South China University of Technology, Guangzhou 510641, China

(Received 2 February 2020; accepted 14 May 2020; published 2 June 2020)

We propose and show that antichiral edge states can be realized in a gyromagnetic photonic crystal (GPC) with a honeycomb lattice consisting of two interpenetrating triangular sublattices *A* and *B*. When sublattices *A* and *B* are immersed in opposite external magnetic fields respectively, the band structure of the GPC tilts and antichiral edge states emerge. These special edge states propagate in the same direction at the two opposite parallel zigzag boundaries of the GPC, which are completely distinguished from the well-studied topological edge states in chiral photonic systems where the edge states transport in opposite directions at the opposite two parallel zigzag boundaries. We show that these unique antichiral edge states originate from the overall coupling effects of the counterclockwise energy flux vortexes of sublattice *A* and clockwise energy flux vortexes of sublattice *B*, so that two copropagating one-way transport channels are created on the boundaries. We further demonstrate that these antichiral edge states are also strongly robust against backscattering from the obstacles at the zigzag edges. Our findings clearly indicate that deeply digging into the GPC systems can help to find rich novel and significant topological physics. Antichiral edge states are of significance not only in basic physics, but also in offering useful insights and routines to design novel electromagnetic and optical functional devices, such as the compact multichannel one-way waveguide.

DOI: 10.1103/PhysRevB.101.214102

I. INTRODUCTION

Topological concepts and physics have inspired tremendous attention and research enthusiasm in science and technology communities in recent decades [1]. The presence of robust interfacial states confined at the boundaries of bulky material with insulating gap have an obvious prospect of potential technological applications. Inspired from the discovery of condensed quantum Hall effect and topological insulator, researchers proposed that it is feasible to make an analogy between photons in photonic crystal (PC) systems and electrons in condensed physics systems, leading to the emergence of topological photonics [2–4]. Researchers have verified various basic concepts of topological physics, such as Weyl points [5–8], nodal lines [9], corner states [10–14], valley states [15–20], and bulk Fermi arc [21] in photonic systems. Moreover, many interesting topological devices, such as multimode one-way waveguides [22,23], high-performance slow-light delay lines [24–26], and dissipationless wave benders [27–30], three-dimensional topological insulators [31], topological lasers [32–35], and on-chip topological waveguides [17,36], have been investigated.

One of the most striking and intriguing ways to produce topological protected electromagnetic (EM) edge states is to immerse a gyromagnetic photonic crystal (GPC) in an external magnetic field to break the time-reversal symmetry [37–46]. These EM edge states generally display the chiral properties that the edge states can only propagate clockwise or counterclockwise along the structure boundary. For example, when the structure is a rectangular or parallelogram, the edge states transport in opposite directions at the two parallel boundaries but not in the same direction. These EM chiral edge states were theoretically predicted by Haldane *et al.* in a two-dimensional (2D) GPC system by analogy to the integer quantum Hall effect in a 2D electron gas system [37,38]. Shortly afterwards, Wang *et al.* [40] and Fu and co-workers [42,43] experimentally observed the EM chiral edge states at microwave domain in a square-lattice 2D GPC. Such a GPC supports EM waves transporting unidirectionally and robustly even in the presence of an inserted metal obstacle. Subsequently, Poo *et al.* [44] experimentally demonstrated that the EM chiral one-way edge states also could exist along the zigzag edges of a honeycomb GPC, and they are also strongly robust against various types of defects and obstacles.

Very recently, there has been growing interest to realize one-way edge states transporting along the same direction on two parallel boundaries (i.e., copropagating edge states), and these special states are called antichiral edge states [47–49]. In 2018, Colomés *et al.* [47] theoretically proposed electronic antichiral edge states through adopting an ingenious but physically unrealistic modification of the Haldane model, where the next-nearest-neighbor hopping term was introduced to act equally in both sublattices. Significantly, the emergence of antichiral edge states enriches the realm of topological physics and arises a wide range of research enthusiasms. In 2019, Bhowmick *et al.* [48] theoretically demonstrated that electronic antichiral edge states could emerge in a honeycomb lattice consisting of Heisenberg ferrimagnets with broken sublattice symmetry, and they made the prediction of potential materials, which may excite electronic antichiral edge states. Very recently, Mandal *et al.* [49] theoretically discussed a photonic antichiral edge state in an exciton-polariton system

---

[*] These authors contributed equally to this work.

[†] Corresponding author: phzyli@scut.edu.cn

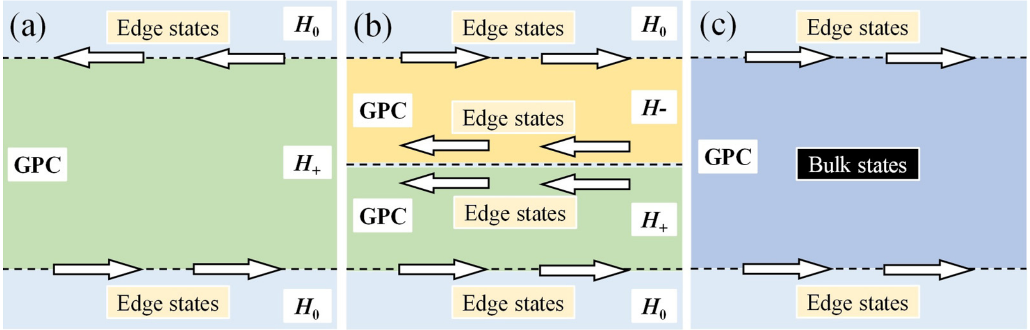

FIG. 1. Schematic illustrations of (a) counterpropagating edge states (single chiral GPC), (b) trivial copropagating edge states (double chiral GPCs), (c) nontrivial copropagating edge states (single antichiral GPC). The arrows indicate the transport directions of the energy fluxes, and the black dotted lines present the interfaces.

by using the polarization-dependent interaction of polariton condensates; Nevertheless, this structure only works in a low-temperature environment in practical experiments. Obviously, the finding of antichiral edge states will open up new opportunities and research fields for topological physics and functionality devices. However, there is still a great challenge to achieve antichiral edge states in fields more diverse than condensed-matter and exciton-polariton systems. Moreover, it is also highly desirable to realize antichiral edge states in a relatively simple structure and without harsh conditions. Fortunately, the GPC system can provide a promising means to attack this challenging issue. In this paper, we propose that antichiral edge states can be realized in a honeycomb GPC consisting of two interpenetrating triangular sublattices A and B, which are immersed in opposite external magnetic fields respectively.

The paper is organized as follows. In Sec. II, we discuss the formation of two copropagating edge states by using two chiral GPCs head by head, and propose a scheme to create copropagating edge states naturally in a single antichiral GPC. In Sec. III, we calculate, plot, and analyze the band diagrams of GPC under three different distributions of external magnetic fields respectively. In Sec. IV, we further depict and discuss the projected band structures for chiral and antichiral edge states. Then, in Sec. V, we demonstrate the transport phenomena of chiral and antichiral edge states and then verify their robustness for obstacles at the zigzag edges along the x direction. Furthermore, in Sec. VI, we generalize the formation mechanism of chiral and antichiral edge states by analyzing their transport behaviors. In Sec. VII, we construct a simpler and more compact three-channel one-way waveguide by using two antichiral GPCs, and further introduce the experimental scheme design of antichiral GPC. Finally, Sec. VIII contains a brief summary of the main findings.

II. MODEL AND METHOD

Generally, the EM chiral edge states exist in a GPC system with broken time-reversal symmetry by applying an external magnetic field [36–43], as shown in Fig. 1(a). There exist edge states on both edges of the GPC, and they transport leftwards and rightwards at the upper and lower boundaries respectively, named as counterpropagating edge states. In order to create edge states propagating rightwards both at the upper and lower parallel boundaries (i.e., copropagating edge states), a natural and simple way is to use two GPCs biased by the opposite external magnetic field respectively, and combine them with each other head by head, as shown in Fig. 1(b). However, owing to the chirality of isolated GPC, other edge states propagating leftwards will exist at the interface between the two GPCs. Obviously, this method to create copropagating edge states is trivial. It is our aim to explore a nontrivial way to create EM copropagating edge states naturally in a single antichiral GPC structure (colored by deep blue), as plotted in Fig. 1(c).

We first construct a 2D GPC consisting of a honeycomb lattice of gyromagnetic cylinders [yttrium-ion-garnet (YIG)] with zigzag edges along the x direction immersed in air, as shown in Figs. 2(a) and 2(b). Besides, the honeycomb lattice can be divided into two interpenetrating triangular lattices composed of second neighbors with π rotation symmetry from each other [i.e., sublattices A and B, marked by the dashed lines in Fig. 2(b)]. The radius of gyromagnetic cylinders is $r = 0.15a$, where $a = 1$ cm is the lattice constant, and the permittivity of YIG is $\varepsilon = 15$.

Numerical simulations in this work are all conducted using the 2D EM waves (frequency domain) module and carried out by finite-element method. In the band diagram calculations for bulk GPC, the unit cell is centered at the point of sixfold rotation symmetry and is bounded by the hexagon of nearest neighbors. All six boundaries of the unit cell are set as Floquet periodic boundaries. Besides, in the projected band-structure calculations for edge states, the parallelogram supercell with zigzag edges along the x direction is used. To ensure the results accurate enough, this supercell includes 24 unit gyromagnetic cylinders in our practical calculations. The upper and lower boundaries of the supercell are set as perfect electric conductors, and the left and right boundaries of the supercell are set as Floquet periodic boundaries. Moreover, in the transport phenomena calculations for edge states, the upper and lower boundaries of the GPC are set as perfect electric conductors, and the left and right boundaries of the GPC are set as scattering boundary conditions. The edge states are excited by two identical point sources at the upper and lower edges respectively.

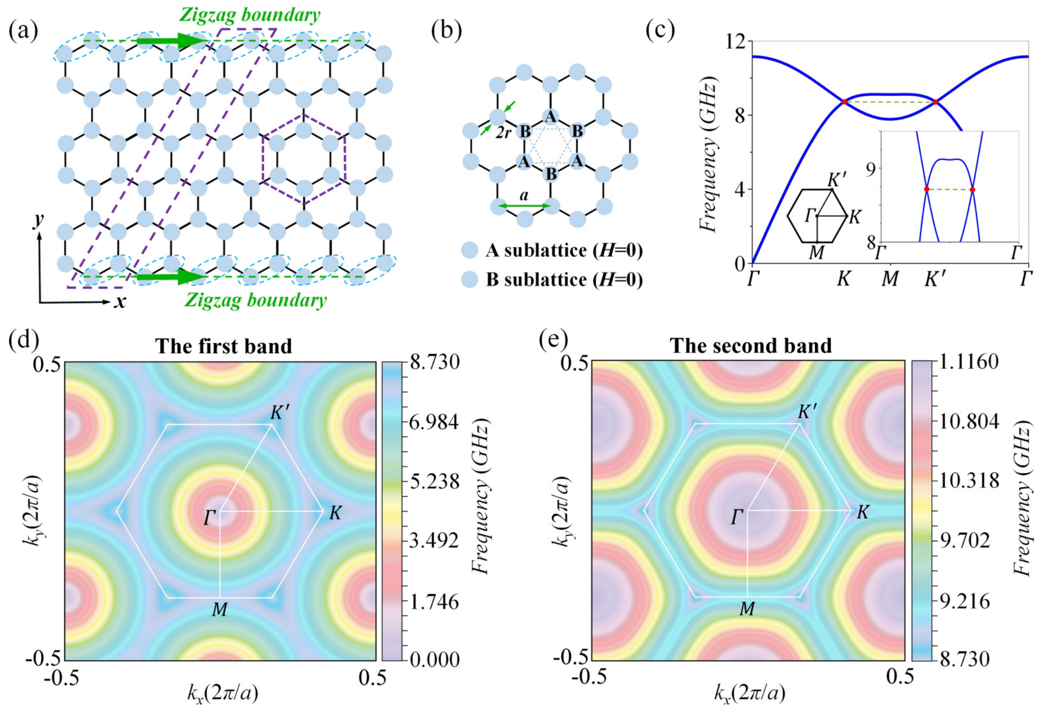

FIG. 2. GPC structure, band structure, and equal frequency curves. (a) GPC Structure with the zigzag edges along x direction. The parallelogram supercell [left side of (a)] and honeycomb unit cell [right side of (a)] are used to calculate the projected band structure and bulk band structure respectively. (b) Schematic diagram of the honeycomb lattice. The light blue dots denote the two sublattices A and B with no external magnetic field applied. (c) Band structure of the honeycomb lattice (bottom left: first Brillouin zone; bottom right: partially enlargement of the band structure). The red dots indicate the two Dirac points which are connected by a green dotted line connects the two Dirac points. (d),(e) Equal frequency curves of the first and second bands, respectively.

III. BAND DIAGRAM FOR BULK GPCs

When the external magnetic field is zero, the permeability of YIG is $\mu = 1$, and gyromagnetic cylinders are colored in light blue in Figs. 2(a) and 2(b). Only E polarization (E is perpendicular to the xoy plane) is considered. Figure 2(c) shows the band structure of the GPC. Obviously, there is no band gap between the first and second bands, as these two bands intersect with each other at two Dirac points of K and K' in the first Brillouin zone [bottom left corner of Fig. 2(c)]. Due to the protection of simultaneous time-reversal and space-reversal symmetries, the band structure is symmetric about the high-symmetry point M. Two Dirac points are marked as red dots and they are connected by a green dotted line [Fig. 2(c)]. The partial enlargement of band structure [bottom right corner of Fig. 2(c)] shows that the frequencies of these two Dirac points are at 8.730 GHz and the slope of the green dotted line is zero. Figures 2(d) and 2(e) show the synthetic pictures of band diagrams constructed by superimposing the first Brillouin zone on the equal frequency curves of the first and second bands, respectively. The equal frequency curves of these two bands possess sixfold rotation symmetry around point Γ at the center of the first Brillouin zone owing to the protection of the sixfold rotation symmetry. Besides, the frequency ranges of the first and second bands are 0–8.730 and 8.730–1.1160 GHz respectively, which are consistent with the calculated results of band structure displayed in Fig. 2(c).

Next, we study the case of the two sublattices A and B both immersed in an external magnetic field of $H_+ = 2200\,\mathrm{G}$, as schematically depicted in Figs. 3(a) and 3(b), where all gyromagnetic cylinders are colored in red. As H_+ is applied along the axis of gyromagnetic cylinders (i.e., $+z$ direction normal to the 2D plane), the strong anisotropy of YIG is induced to produce a permeability tensor [22,23],

$$\hat{\mu} = \begin{pmatrix} \mu_r & i\mu_k & 0 \\ -i\mu_k & \mu_r & 0 \\ 0 & 0 & 1 \end{pmatrix},$$

where $u_r = 0.84$, $u_k = 0.41$. Due to the presence of nondiagonal imaginary parts in the permeability tensor, the time-reversal symmetry of GPC is broken. Figure 3(c) shows that the degeneracy of Dirac points K and K' are lifted up, so that the first and second bands separate from each other, and then a full band gap emerges (green zone). The partial enlargement of the band structure [bottom-right corner of Fig. 3(c)] shows that the frequency range of this band gap (green zone) extends from 8.900 to 9.130 GHz (the band gap width is 0.230 GHz). Besides, Figs. 3(d) and 3(e) show the equal frequency curves of the first and second bands in the frequency ranges of 0–8.900 and 9.130–11.710 GHz respectively. They still possess a sixfold rotation symmetry around point Γ at the center of the first Brillouin zone, owing to the protection of the sixfold rotation symmetry.

We proceed to study the case of two interpenetrating triangular sublattices A and B applied with $H_+ = 2200\,\mathrm{G}$ and $H_- = -2200\,\mathrm{G}$ respectively, as shown in Figs. 4(a) and 4(b). The gyromagnetic cylinders of sublattices A and B are marked

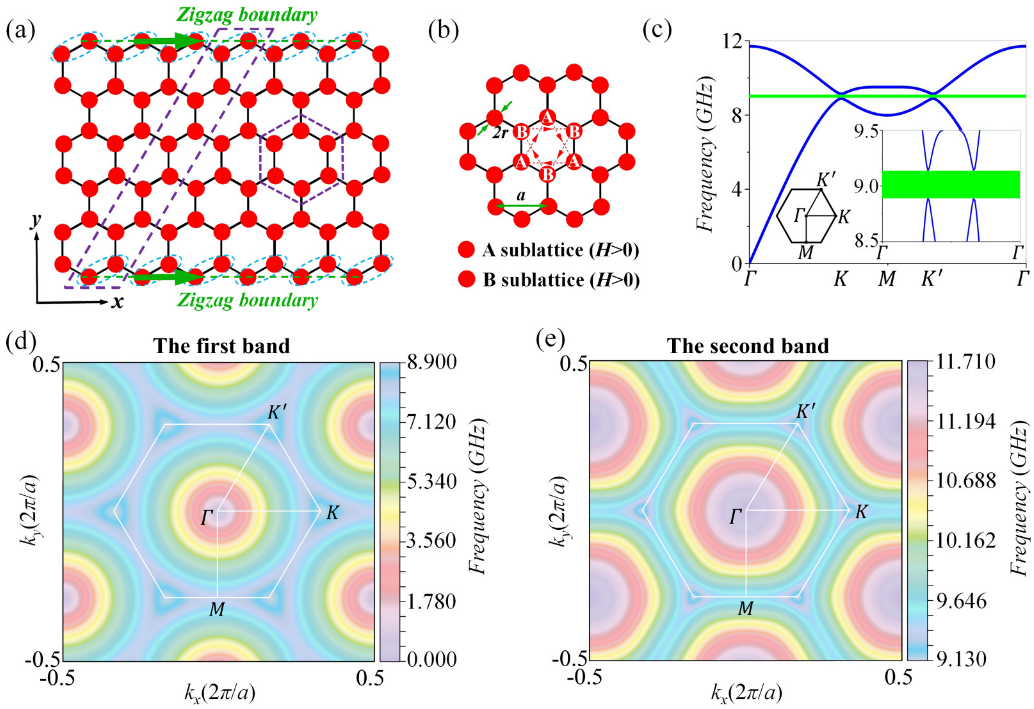

FIG. 3. GPC structure, band structure and equal frequency curves. (a) Structure of GPC with the zigzag edges along x direction. The parallelogram supercell [left side of (a)] and honeycomb unit cell [right side of (a)] are used to calculate the projected band structure and bulk band structure respectively. (b) Schematic diagram of honeycomb lattice. The red dots denote the two sublattices A and B with $H_+= 2200$ G applied simultaneously. (c) Band structure of honeycomb lattice (bottom left: first Brillouin zone; bottom right: partially enlargement of the band structure). Green rectangle indicates the full band gap. (d),(e) Equal frequency curves of the first and second bands, respectively.

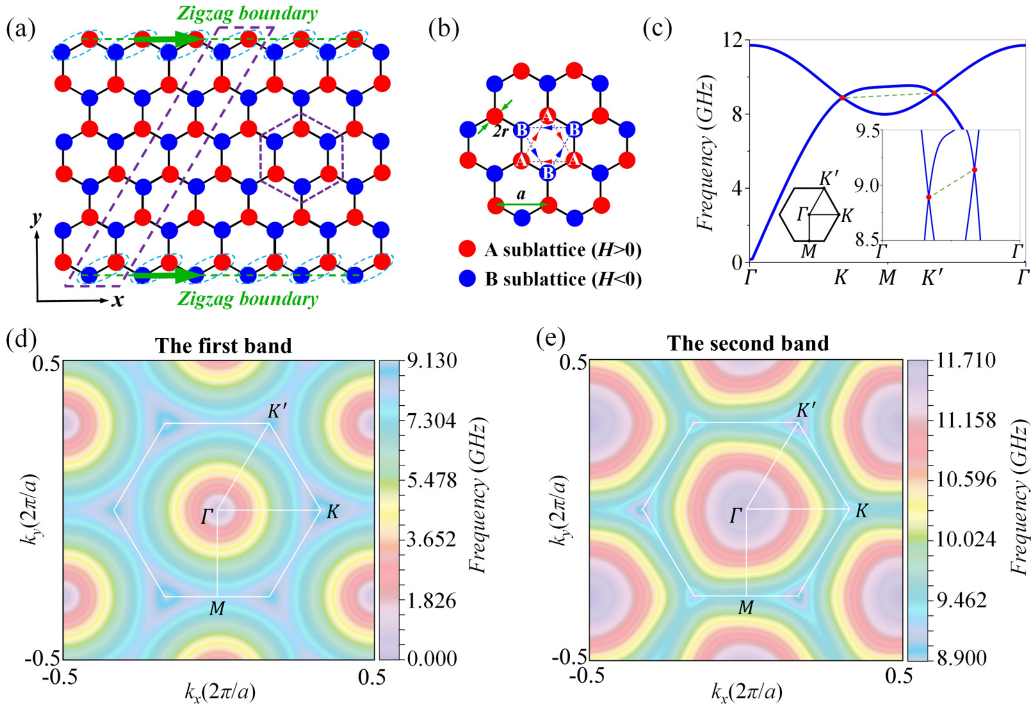

FIG. 4. GPC structure, band structure, and equal frequency curves. (a) Structure of GPC with the zigzag edges along x direction. The parallelogram supercell [left side of (a)] and honeycomb unit cell [right side of (a)] are used to calculate the projected band structure and bulk band structure respectively. (b) Schematic diagram of honeycomb lattice. The red and blue dots denote that two sublattices A and B are applied with $H_+ = 2200$ G and $H_- = -2200$ G respectively. (c) Band structure of honeycomb lattice (bottom left: first Brillouin zone; bottom right: partially enlargement of the band structure). Red dots indicate the two Dirac points which are connected by a green dotted line. (d),(e) Equal frequency curves of the first and second bands, respectively.

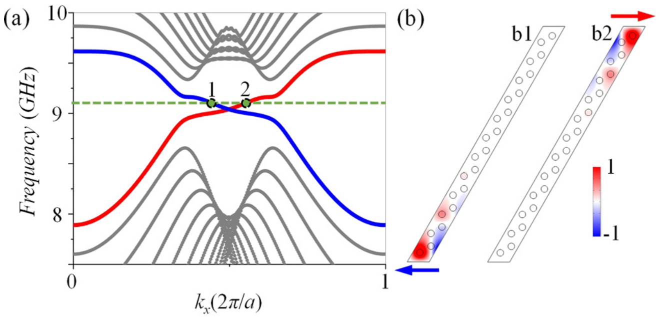

FIG. 5. Projected band structures and eigenmodal fields of the chiral edge states. (a) Projected band structures of the YIG in Fig. 3(a). (b) Eigenmodal fields of points 1 and 2 denoted in (a). The red and blue arrows indicate edge states propagating rightwards and leftwards respectively.

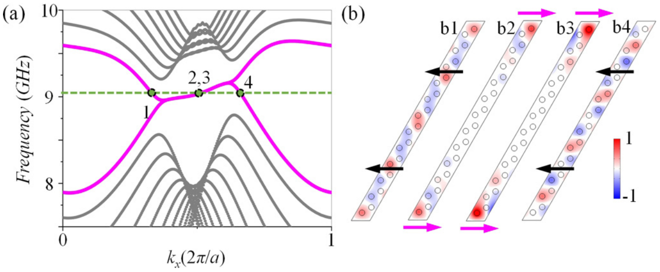

FIG. 6. Projected band structures and eigenmodal fields of antichiral edge states. (a) Projected band structures of the YIG in Fig. 4(a). (b) Eigenmodal fields of points 1, 2, 3, and 4 in (a). Magenta arrows indicate edge states propagating rightwards, while black arrows denote bulk states transporting leftwards.

in red and blue respectively. Figure 4(c) shows that the first and second bands are not separated from each other and still intersect at Dirac points K and K'. However, the band structure tilts and loses the symmetry about point M in the first Brillouin zone because the Dirac points at K and K' move down and up respectively. To see more conspicuously the tilt of the band structure, a green dotted line is used to connect these two intersecting points. Obviously, the slope of the dotted line is a positive value instead of zero. Besides, the frequencies at points K and K' are 8.900 and 9.130 GHz respectively, and their difference is 0.230 GHz, which is consistent with the band-gap width of Fig. 3(c). Figures 4(d) and 4(e) show that due to the breaking of the sixfold rotation symmetry, the equal frequency curves of the first and second bands lose the sixfold rotation symmetry around point Γ, and they are divided into two sets of triangular rotation symmetry with π rotation symmetry different from each other. Points K and K' are shifted downwards and upwards respectively to create tilted band structures. It should be noted that the frequency range of the first and second bands are 0–9.130 and 8.900–11.710 GHz respectively, which are consistent with the calculation results of band structure in Fig. 4(c).

IV. PROJECTED BAND STRUCTURES FOR CHIRAL AND ANTICHIRAL EDGE STATES

Now, we consider the projected band structures of the honeycomb GPC system with zigzag edges along the x direction to study the properties of edge states, and predict the transport behaviors of EM waves by analyzing their eigenmodal fields. We first consider the case of Fig. 3(a) where the GPC is immersed in $H_+ = 2200\,\mathrm{G}$. Figure 5(a) shows the projected band structure of the GPC. The whole band structure is symmetrical about $k_x = 1/2$, and two dispersion curves (colored in blue and red respectively) appear inside the band gap and they intersect with each other at $k_x = 1/2$. Generally, the signs of the slopes of dispersion curves represent the transport directions of their eigenmodal fields. Thus, the eigenmodal fields corresponding to the red and blue dispersion curves in the band gap will transport in positive (right side) and negative (left side) directions, respectively. The eigenmodal fields of points 1 and 2 (green points) at 9.050 GHz are depicted in Fig. 5(b). Obviously, they both are one-way edge states, since the slopes at points 1 and 2 are negative and positive respectively in the whole first Brillouin zone as shown in Fig. 5(a). Specifically, the EM wave corresponding to points 1 and 2 will transport leftwards (blue arrow) and rightwards (red arrow) along the lower and upper boundaries respectively, as shown in Fig. 5(b). In other words, the EM edge states will transport along two parallel boundaries in opposite directions, which show the chirality of edge state in this GPC system clearly.

We further study the case of Fig. 4(a) where the two sublattices A and B are subject to application of magnetic field with $H_+ = 2200\,\mathrm{G}$ and $H_- = -2200\,\mathrm{G}$ respectively. Figure 6(a) shows the projected band structure of the GPC. The whole band structure tilts and loses symmetry about $k_x = 1/2\ (2\pi/a)$. There exist two mutually intersecting dispersion curves (colored in magenta), and they are degenerate with each other around $k_x = 1/2\ (2\pi/a)$, i.e., possessing the identical dispersion. The eigenmodal field profiles of points 1–4 (green points) at 9.050 GHz are plotted in Figs. 6(b1)–6(b4), respectively. Figures 6(b1) and 6(b4) show that the eigenmodal fields of points 1 and 4 are both dispersed uniformly in the bulk and thus they are dispersive bulk states in the GPC. It should be pointed out that as time elapses, they will transport leftwards continuously (black arrows), which is in accordance with the facts that the slopes of the dispersion curves at points 1 and 4 are both negative. However, Figs. 6(b2) and 6(b3) show that the eigenmodal fields at points 2 and 3 are primarily concentrated on both edges of the GPC and thus they are localized edge states against the GPC. Being completely different from the case of chiral edge state in Fig. 5(b), as time elapses, these two edge states will both transport rightwards (magenta arrows), in accordance with the positive slopes of the dispersion curves at points 2 and 3. These features clearly indicate that there indeed exist edge states propagating in the same direction at both parallel boundaries of the designed GPC, clearly confirming the existence of antichirality. Besides, these antichiral edge states are accompanied by minor bulk states to provide necessary counterpropagating energy fluxes for balance. It should be noted that the intensities of edge states [Figs. 6(b2) and 6(b3)] are greater than those of bulk states [Figs. 6(b1) and 6(b4)] on both boundaries of the GPC. Therefore, it is expected that the antichiral edge states

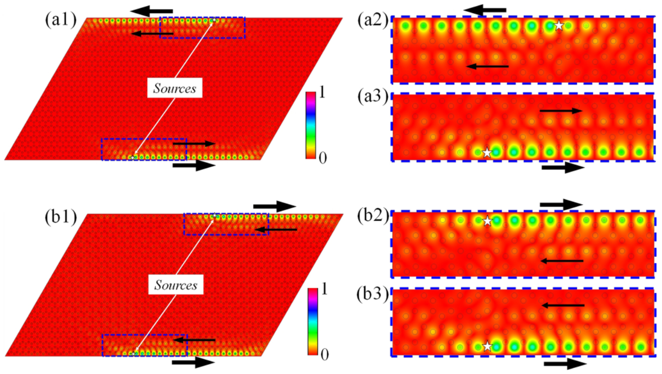

FIG. 7. Transport phenomena of chiral and antichiral edge states without metallic obstacles: (a1)–(a3) chiral edge states, (b1)–(b3) antichiral edge states. The thick and thin black arrows indicate the main and secondary transport channels of energy fluxes, respectively. The white stars with black frame are sources.

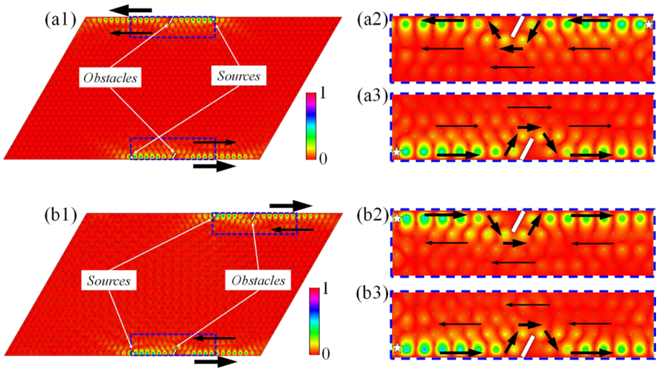

FIG. 8. Transport phenomena of chiral and antichiral edge states with the rectangular metallic obstacles: (a1)–(a3) chiral edge states, (b1)–(b3) antichiral edge states. The thick and thin black arrows indicate the main and secondary transport channels of energy fluxes, respectively. The white stars with black frame denote sources.

will dominate the bulk states when point sources radiating at 9.050 GHz are placed on the boundaries.

V. TRANSPORT ROBUSTNESS OF CHIRAL AND ANTICHIRAL EDGE STATES

So far, we have discussed the existences of chiral and antichiral edge states by analyzing their band structures and eigenmodal fields. Next, we construct a honeycomb GPC parallelogram ribbon with two zigzag edges (i.e., the upper and lower edges) along the x direction to excite chiral and antichiral edge states to see their transport behaviors. As shown in Fig. 7, two point sources (white stars) are located at the upper and lower zigzag edges, respectively, and they both oscillate at 9.050 GHz. The upper and lower boundaries of the structure are perfect electric conductors to avoid energy fluxes radiating into air, while the left and right boundaries of the structure are set as scattering boundary condition. When all YIG cylinders are biased by $H_+ = 2200\,\mathrm{G}$ [Fig. 3(a)], there exist two edge states only transporting rightwards and leftwards at upper and lower edges respectively, i.e., counterpropagating, which shows the chirality [Fig. 7(a1)]. The partially enlarged field pattern at the upper and lower boundaries are shown in Figs. 7(a2) and 7(a3), respectively. There exist two transport channels, i.e., the main and secondary channels. The majority of energy fluxes transport leftwards (or rightwards) along the upper (or lower) zigzag edge, forming the main channel (thick black arrows). The minority of energy fluxes also propagate in the same direction with the main channel at some distance below the inner edges, forming the secondary channel (thin black arrows).

When the two triangular sublattices A and B are immersed in $H_+ = 2200\,\mathrm{G}$ and $H_- = -2200\,\mathrm{G}$ respectively [Fig. 4(a)], we find that there exist edge states at the upper and lower boundaries of the parallelogram structure respectively, and they both transport rightwards, i.e. copropagating, showing the antichirality [Fig. 7(b1)]. The partially enlarged field patterns at the upper and lower boundaries are shown in Figs. 7(b2) and 7(b3), respectively. There also exist two transport channels (i.e., the main and secondary channels). However, the energy fluxes of the main and secondary channels are opposite, i.e., the energy fluxes of the main channel transport rightwards along the upper and lower zigzag edges, while the energy fluxes of the secondary channel propagate leftwards at some distance below the inner edges. These transport phenomena are completely consistent with the calculation and analysis results of eigenmodal fields illustrated in Fig. 6.

As is well known, the unique property of the topological edge state is its robust transport immune against perturbations and obstacles at the path. To demonstrate the robustness of chiral and antichiral edge states, two metallic rectangular obstacles with length of $1.5a$ and thickness of $0.2a$ are inserted at both zigzag edges respectively, as shown in Figs. 8(a1)–8(a3) and 8(b1)–8(b3). The majority of energy fluxes are still strongly concentrated at edges and transport forwards along the main channels, and the minority of energy fluxes propagate along the secondary channel. Importantly, no matter whether they are chiral or antichiral edge states, their energy fluxes both can go around the obstacles and transport forwards with almost no backscattering, showing excellent robustness.

VI. PHYSICAL MECHANISMS UNDERLYING THE FORMATION OF CHIRAL AND ANTICHIRAL EDGE STATES

To observe and compare the transport behaviors of chiral and antichiral edge states in detail, Figs. 9 and 10 plot the detailed distributions of energy fluxes (magenta arrows) along the upper and lower edges corresponding to the field patterns displayed in Figs. 7 and 8, respectively. The magenta arrows are used to reflect explicitly the intensities and directions of energy fluxes, i.e., the Poynting vector. Since the strong circulation of energy fluxes around each single gyromagnetic cylinder are excited, for convenience, the counterclockwise and clockwise rotating energy fluxes are respectively marked as blue and green circular arrows, with their thicknesses used to represent the relative intensities of energy flux. Besides, the main and secondary transport channels are marked as the thick and thin black arrows, respectively.

Very recently, Chen *et al.* proposed a left-hand law to describe the transport directions of the EM wave in

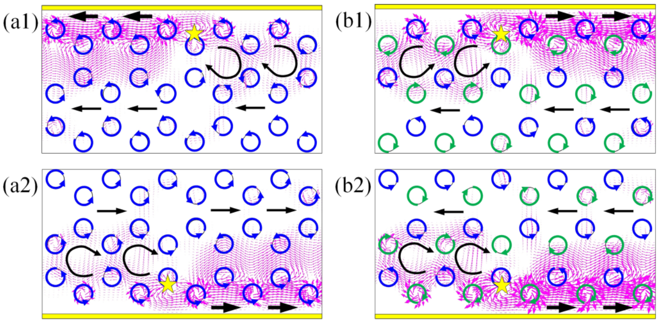

FIG. 9. Distributions of energy fluxes (Poynting vector, marked as the magenta arrows) of the edge states without metallic obstacles: (a1),(a2) chiral edge states. (b1),(b2) antichiral edge states. (a1),(b1) and (a2),(b2) are the cases of upper and lower edges respectively. The yellow stars indicate the sources at zigzag edges.

gyromagnetic materials [50]. According to the left-hand law, when gyromagnetic cylinders used in this work are immersed in $H_+ = 2200\,\mathrm{G}$, due to $B(H_+) = \mu_k/\mu_r = 0.488 > 0$, an EM wave around gyromagnetic cylinders will rotate counterclockwise. In contrast, when they are biased by $H_- = -2200\,\mathrm{G}$, $B(H_-) = -\mu_k/\mu_r = -0.488 < 0$, and the rotating direction will be clockwise. As shown in Fig. 9, the Poynting vector distributions of each single gyromagnetic cylinder are completely consistent with the predicted results of Ref. [50]. On one hand, for chiral edge states in Figs. 9(a1) and 9(a2), where all gyromagnetic cylinders are immersed in $H_+ = 2200\,\mathrm{G}$, the direction of the EM wave traveling around gyromagnetic cylinders is counterclockwise. Under the overall coupling effects of counterclockwise energy vortexes, the main and secondary channels can only support energy fluxes in one direction. Especially, the minority of energy radiating backwards is completely towed back to propagate forwards via a counterclockwise loop along the inner edges of the whole hexagon.

On the other hand, for antichiral edge states in Figs. 9(b1) and 9(b2), because sublattices A and B are applied with opposite external magnetic field respectively, the energy fluxes are counterclockwise and clockwise cycling around the gyromagnetic cylinders of A and B lattices respectively. For the upper edge [Fig. 9(b1)], the energy fluxes are counterclockwise cycling (blue circular arrows) around the odd rows of gyromagnetic cylinders (the first row is at upper edge site), while the energy flux vortexes of even rows of gyromagnetic cylinders are clockwise (green circular arrows). These microscopic energy flux vortexes finally form the unique macroscopic transport phenomena, that is, the vast majority of energy fluxes propagate rightwards along the main channel, whereas the small part of the energy fluxes transport leftwards along the secondary channel. Besides, at the first glance it seems that the main and secondary channels are in spatial separation, but actually, the energy fluxes of edge states are not independent when transporting along the main and secondary channels. They couple with each other to propagate rightwards during the transport process. Thus, the backscattering of the antichiral edge states is nearly suppressed in this honeycomb GPC structure. Conversely, for the lower edge [see Fig. 9(b2)], the energy fluxes are clockwise (or counterclockwise) cycling around the odd (or even) rows of gyromagnetic cylinders (the first row is at lower edge site), and these microscopic energy flux vortexes finally form the energy fluxes macroscopically propagating rightwards.

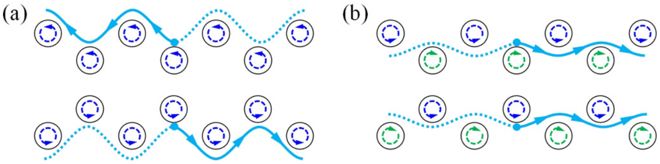

Chiral edge states		Antichiral edge states

FIG. 10. Schematic diagrams of physical mechanism. (a) Chiral edge states, (b) antichiral edge states. The blue and green circular dotted arrows denote the counterclockwise and clockwise energy vortexes around gyromagnetic cylinders respectively.

It should be noted that the directions of energy flux vortexes around the gyromagnetic cylinders at the odd or even rows of the upper boundary are opposite from those of the lower boundary [see Figs. 9(b1) and 9(b2)]. These are completely different from the cases of chiral edge states where the energy flux vortex directions of all gyromagnetic cylinders are counterclockwise [see Figs. 9(a1) and 9(a2)]. We further depict the physical pictures of the formation mechanism of chiral and antichiral edge states by simplifying the distributions of energy fluxes, as shown in Fig. 10. For the chiral edge states [see Figs. 10(a)], the overall coupling effects of the counterclockwise energy vortexes result in the feature that the upper or lower zigzag edges only support the energy fluxes transporting rightwards or leftwards respectively, while for the antichiral edge states [see Figs. 10(b)], since the energy flux cycling around the gyromagnetic cylinders of sublattices A and B are counterclockwise and clockwise respectively, two one-way transport channels are created between A and B gyromagnetic cylinders along the boundaries. Besides, the energy vortexes of gyromagnetic cylinders at the upper and lower boundaries are opposite (i.e., the symmetry of sublattices are broken), as a result, these two one-way transport channels only support the energy fluxes propagating rightwards, resulting in the antichiral edge states.

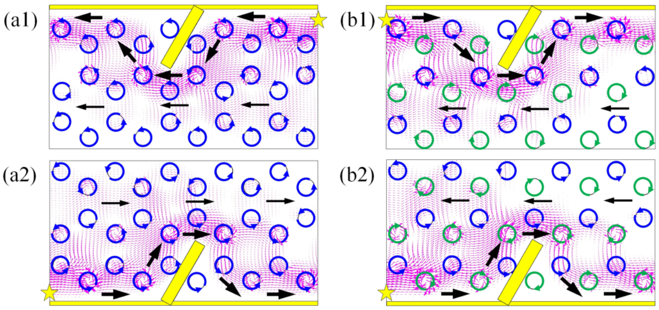

FIG. 11. Distributions of energy fluxes (Poynting vector, marked as the magenta arrows) of the edge states with metallic rectangular obstacles at the zigzag edge: (a1),(a2) chiral edge states. (b1),(b2) antichiral edge states. (a1),(b1) and (a2),(b2) are the cases of upper and lower edges respectively. Yellow stars and rectangles indicate the sources and obstacles respectively.

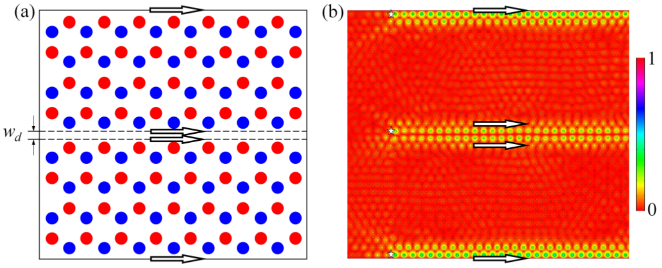

FIG. 12. Three-channel one-way waveguide: (a) schematic illustration, (b) simulated result. Three point sources (marked as white stars) radiating at 9.050 GHz are placed on the boundaries.

We use the following physical picture to understand the robust transport feature of both chiral and antichiral edge states. When the metallic rectangular obstacles (colored in yellow) are inserted into the zigzag edges, as shown in Fig. 11, the energy fluxes still only transport rightwards (or leftwards) in the form of the microscopic energy flux vortexes as mentioned above, and an equivalent transport channel is created between the obstacle and GPC. The energy fluxes move rightwards along the equivalent channel to go around the metallic obstacle. Especially, for antichiral edge states, although there is still a small amount of energy fluxes transporting leftwards in the inner edges due to the clockwise vortexes, they are coupled back into the main channel to transport rightwards, resulting in the nearly perfect transport of energy fluxes even if there exists a metallic obstacle. Besides, there are four boundary types in honeycomb photonic crystal, i.e., zigzag, bearded zigzag, armchair, and bearded armchair boundaries, obtained by cutting the honeycomb lattice in different directions. However, it should be emphasized that only the zigzag boundary has the antichiral edge state.

VII. APPLICATION AND EXPERIMENTAL DESIGN

As we know, the topological photonic chiral state may pave the way to the integrated one-way photonic circuits, because such a chiral state propagates unidirectionally and its transmission is immune to large metallic scatters and defects. In these one-way photonic circuits, EM waves travel inside the waveguide channels and they are located at the topological photonic crystal boundaries. For a single chiral topological photonic crystal with two parallel boundaries, only one boundary can be utilized to transport energy fluxes from the left side to the right side, owing to their chirality. If one hopes to design an integrated photonic circuit with multiple one-way channels for EM waves transporting from the left side to the right side, it is necessary to use many chiral topological photonic crystals, which would be very costly and bulky. However, thanks to the antichiral topological photonic crystals, it is possible to transfer EM waves in a multichannel one-way waveguide with a simpler and more compact structure.

Here we exhibit the unique advantages and applications of antichiral edge state by constructing a three-channel unidirectional waveguide. Figure 12 shows that antichiral GPC can be used to construct such a three-channel one-way waveguide in a natural and simple way, owing to the copropagating properties of antichiral edge states. We combine two antichiral GPCs with each other head by head to construct a three-channel waveguide with certain waveguide width ($w_d = 1.5\,\text{mm} = 0.15a$), as shown in Fig. 12(a). Figure 12(b) shows that three independent channels indeed can simultaneously support the EM wave transporting rightwards unidirectionally. However, it is impossible to construct a three-channel one-way waveguide by combining two chiral GPCs in any form (at least three chiral GPCs are required), owing to the chirality of these isolated GPCs. Thus, the existence of the antichiral edge state may provide a great potential to promote a more compact multichannel one-way waveguide structure, improve the utilization efficiency of the waveguide channels, and increase the transmission amount of energy fluxes.

So far, we have theoretically analyzed the implementation of antichiral edge states of GPCs in detail. Here we would like to propose a realistic experimental design to observe the aforementioned phenomena. Two metallic slabs are set in the upper and lower parts of the GPC structure and they are carved out as honeycomb arrays respectively, but they are not completely hollowed out and leave a certain thickness (d) [see Fig. 13(b)], in order to forbid the electromagnetic waves from leaking and transporting in the z direction. A pair of honeycomb magnet arrays are pressed into the honeycomb holes in metallic slabs (made from nonmagnetic metals, such as aluminum alloy) above and below the YIG structure respectively, to avoid the displacement of magnets owing to the attraction and repulsion of different magnets. The positive and negative magnetic fields are produced by the different combinations of the magnetic pole respectively, as shown in Fig. 13(b). Similar

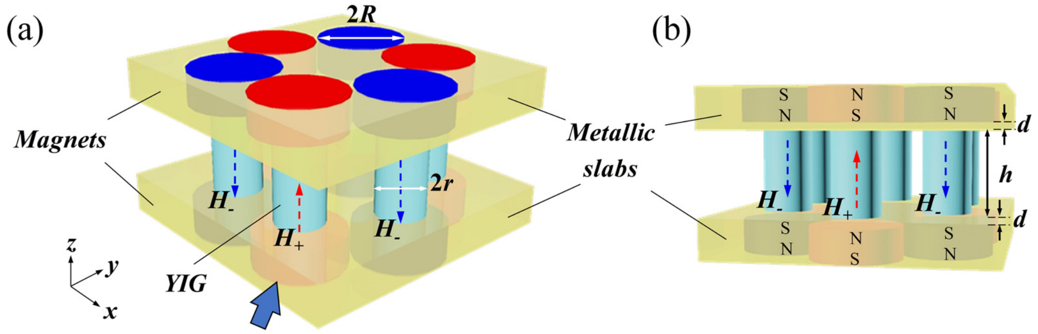

FIG. 13. Experimental scheme design. (a) Schematic diagrams of a unit cell. (b) Side view of (a); the angle of view is the direction marked by the blue arrow in (a).

schemes were utilized in Refs. [51,52]. Besides, to produce as uniform a magnetic field strength as possible along the YIG cylinders (i.e., $+z$ direction), the magnet should be designed to be a cylindrical shape with its radii larger than those of YIG cylinders (i.e., $R > r$). Furthermore, to reduce the attenuation of magnetic fields along the $+z$ direction and the influence of the demagnetization factor, the surface magnetic field strength of magnets in experiment should be larger than that used in simulations.

VIII. CONCLUSIONS

In summary, we have proposed that a honeycomb GPC composed of two interpenetrating triangular sublattices A and B of YIG cylinders can realize antichiral edge states, i.e., create the copropagating edge states in a single GPC. We have considered three different configurations of external magnetic field distributions, which are applied to the GPC. In the first configuration, when the GPC is not magnetized, the first and second bands intersect each other at two Dirac points owing to the protection of simultaneous time-reversal and space-reversal symmetries. In the second configuration, when the GPC is biased by an external magnetic field, the time-reversal symmetry is broken, the degeneracy of Dirac points are lifted up, and the chiral edge states (i.e., counterpropagating edge states) emerge in the full band gap. Remarkably in the third configuration, we have found that when sublattices A and B of the honeycomb GPC are applied with opposite external magnetic fields respectively, the band structure of the GPC tilts and leads to the emergence of antichiral edge states (i.e., copropagating edge states). Significantly, through observing the energy flux distributions of the chiral and antichiral edge states, we have found that the antichiral edge states, similar to the chiral edge states, are also strongly robust against the backscattering from obstacles located at the zigzag edges.

Furthermore, we have analyzed the formation mechanisms and depicted the physical pictures for the chiral and antichiral edge states. We show that the overall coupling effects of the counterclockwise energy flux vortexes cycling around each YIG cylinder will result in the formation of chiral edge states, i.e., counterpropagating edge states, where the upper and lower zigzag edges only support the energy fluxes transporting rightwards and leftwards respectively. In contrast, the overall coupling effects of the counterclockwise energy flux vortexes of sublattice A and clockwise energy flux vortexes of sublattice B will lead to the formation of antichiral edge states, namely, two copropagating one-way transport channels are created on the opposite boundaries of the GPC. Finally, we have created the three-channel one-way waveguide with a simpler and more compact structure by two antichiral GPCs, and designed the experiment scheme to construct the antichiral GPC.

Our findings indicate that the GPC system as one of the most promising ways to create topological chiral edge states also can be used to achieve the antichiral edge states in a relatively simple structure and without harsh conditions. Most importantly, our implementation of antichiral edge states (i.e., copropagating edge states) may offer useful hints to explore deeply fruitful electromagnetic and optical states, properties, and phenomena of nontrivial physical significance in topological photonic structures and systems. The antichiral edge state on which we focus to investigate as a special type of one-way edge state, besides its significance in basic physics, is also promising for practical applications requiring deliberate manipulation of the propagation of EM waves. It can also offer useful insights and routines for designing photonic devices from microwave to optical waves, such as multichannel tunable optical switches and dynamically reconfigurable logic devices.

ACKNOWLEDGMENTS

The authors are grateful for the financial support from the National Natural Science Foundation of China (Grants No. 11974119 and No. 11504114), Science and Technology Program of Guangzhou (Grant No. 201904010105), Guangdong Innovative and Entrepreneurial Research Team Program (Grant No. 2016ZT06C594), Dongguan Introduction Program of Leading Innovative and Entrepreneurial Talents, National Key R&D Program of China (Grant No. 2018YFA 0306200), and Fundamental Research Funds for the Central Universities (Grant No. 2019ZD50).

---

[1] M. Z. Hasan and C. L. Kane, Colloquium: Topological insulators, Rev. Mod. Phys. **82**, 3045 (2010).

[2] M. C. Rechtsman, Y. Plotnik, Y. Segev, M. Segev, M. J. Zeuner, and A. Szameit, Photonic topological insulators, Nat. Mater. **12**, 233 (2013).

[3] L. Lu, J. D. Joannopoulos, and M. Soljačić, Topological photonics, Nat. Photon. **8**, 821 (2014).

[4] A. B. Khanikaev and G. Shvets, Two-dimensional topological photonics, Nat. Photon. **11**, 763 (2017).

[5] L. Lu, Z. Y. Wang, D. X. Ye, L. X. Ran, L. Fu, J. D. Joannopoulos, and M. Soljačić, Experimental observation of Weyl points, Science **349**, 622 (2015).

[6] M. Xiao, Q. Lin, and S. Fan, Hyperbolic Weyl Point in Reciprocal Chiral Metamaterials, Phys. Rev. Lett. **117**, 057401 (2016).

[7] W. J. Chen, M. Xiao, and C. T. Chan, Photonic crystals possessing multiple Weyl points and the experimental observation of robust surface states, Nat. Commun. **7**, 13038 (2016).

[8] L. Lu, L. Fu, J. D. Joannopoulos, and M. Soljačić, Weyl points and line nodes in gapless gyroid photonic crystals, Nat. Photon. **7**, 294 (2017).

[9] W. L. Gao, B. Yang, B. Tremain, H. C. Liu, Q. H. Guo, L. B. Xia, A. P. Hibbins, and S. Zhang, Experimental ovservation of photonic nodal line degeneracies in metacrystals, Nat. Commun. **9**, 950 (2018).

[10] B. Y. Xie, H. F. Wang, H. X. Wang, X. Y. Zhu, J. H. Jiang, M. H. Lu, and Y. F. Chen, Second-order photonic topological insulator with corner states, Phys. Rev. B **98**, 205147 (2018).

[11] Y. Ota, F. Liu, R. Katsumi, K. Watanabe, K. Wakabayashi, Y. Arakawa, and S. Iwamoto, Photonic crystal nanocavity based on a topological corner state, Optica **6**, 786 (2019).

[12] X. D. Chen, W. M. Deng, F. L. Shi, F. L. Zhao, M. Chen, and J. W. Dong, Direct Observation of Corner States in Second-Order Topological Photonic Crystal Slabs, Phys. Rev. Lett. **122**, 233902 (2019).

[13] A. E. Hassan, F. K. Kunst, A. Moritz, G. Andler, E. J. Bergholtz, and M. Bourennane, Corner states of light in photonic waveguides, Nat. Photon. **13**, 697 (2019).

[14] X. W. Luo and C. Zhang, Higher-Order Topological Corner States Induced by Gain and Loss, Phys. Rev. Lett. **123**, 073601 (2019).

[15] J. W. Dong, X. D. Chen, H. Zhu, Y. Wang, and X. Zhang, Valley photonic crystals for control of spin and topology, Nat. Mater. **16**, 298 (2017).

[16] M. I. Shalaev, W. Walasik, A. Tsukernik, Y. Xu, and N. M. Litchinitser, Robust topologically protected transport in photonic crystals at telecommunication wavelengths, Nat. Nanotechnol. **14**, 31 (2019).

[17] X. T. He, E. T. Liang, J. J. Yuan, H. Y. Qiu, X. D. Chen, F. L. Zhao, and J. W. Dong, A silicon-on-insulator slab for topological valley transport, Nat. Commun. **10**, 872 (2019).

[18] F. Gao, H. Xue, Z. Yang, K. Lai, Y. Yu, X. Lin, Y. Chong, G. Shvets, and B. Zhang, Topologically protected refraction of robust kink states in valley photonic crystals, Nat. Phys. **14**, 140 (2018).

[19] Y. Kang, X. Ni, X. Cheng, A. B. Khanikaev, and A. Z. Genack, Pseudo-spin–valley coupled edge states in a photonic topological insulator, Nat. Commun. **9**, 3029 (2018).

[20] J. Noh, S. Huang, K. P. Chen, and M. C. Rechtsman, Observation of Photonic Topological Valley Hall Edge States, Phys. Rev. Lett. **120**, 063902 (2018).

[21] H. Zhou, C. Peng, Y. Yoon, C. W. Hsu, K. A. Nelson, L. Fu, J. D. Joannopoulos, M. Soljačić, and B. Zhen, Observation of bulk Fermi arc and polarization half charge from paired exceptional points, Science **359**, 1009 (2018).

[22] S. A. Skirlo, L. Lu, and M. Soljačić, Multimode One-Way Waveguides of Large Chern Numbers, Phys. Rev. Lett. **113**, 113904 (2014).

[23] S. A. Skirlo, L. Lu, Y. Igarashi, Q. Yan, J. Joannopoulos, and M. Soljačić, Experimental Observation of Large Chern Numbers in Photonic Crystals, Phys. Rev. Lett. **115**, 253901 (2015).

[24] Y. Yang, Y. Poo, R. X. Wu, Y. Gu, and P. Chen, Experimental demonstration of one-way slow wave in waveguide involving gyromagnetic photonic crystals, Appl. Phys. Lett. **102**, 231113 (2013).

[25] J. Chen, W. Liang, and Z. Y. Li, Strong coupling of topological edge states enabling group-dispersionless slow light in magneto-optical photonic crystals, Phys. Rev. B **99**, 014103 (2019).

[26] J. Chen, W. Liang, and Z. Y. Li, Switchable slow light rainbow trapping and releasing in strongly coupling topological photonic systems, Photonics Res. **7**, 1075 (2019).

[27] C. He, X. L. Chen, M. H. Lu, X. F. Li, W. W. Wan, X. S. Qian, R. C. Yin, and Y. F. Chen, Tunable one-way cross-waveguide splitter based on gyromagnetic photonic crystal, Appl. Phys. Lett. **96**, 111111 (2010).

[28] S. Liu, W. Lu, Z. Lin, and S. T. Chui, Magnetically controllable unidirectional electromagnetic waveguiding devices designed with metamaterials, Appl. Phys. Lett. **97**, 201113 (2010).

[29] Y. Poo, R. X. Wu, S. Liu, Y. Yang, Z. Lin, and S. T. Chui, Experimental demonstration of surface morphology independent electromagnetic chiral edge states originated from magnetic plasmon resonance, Appl. Phys. Lett. **101**, 081912 (2012).

[30] Q. B. Li, Z. Li, and R. X. Wu, Bending self-collimated one-way light by using gyromagnetic photonic crystals, Appl. Phys. Lett. **107**, 241907 (2015).

[31] Y. Yang, Z. Gao, H. Xue, L. Zhang, M. He, Z. Yang, R. Singh, Y. Chong, B. Zhang, and H. Chen, Realization of a three-dimensional photonic topological insulator, Nature (London) **565**, 622 (2019).

[32] G. Harari, M. A. Bandres, Y. Lumer, M. C. Rechtsman, Y. D. Chong, M. Khajavikhan, D. N. Christodoulides, and M. Segev, Topological insulator laser: Theory, Science **359**, eaar4003 (2018).

[33] M. A. Bandres, S. Wittek, G. Harari, M. Parto, J. Ren, M. Segev, D. N. Christodoulides, and M. Khajavikhan, Topological insulator laser: Experiments, Science **359**, eaar4005 (2018).

[34] Y. Ota, R. Katsumi, K. Watanabe, S. Iwamoto, and Y. Arakawa, Topological photonic crystal nanocavity laser, Commun. Phys. **1**, 86 (2018).

[35] Z. K. Shao, H. Z. Chen, S. Wang, X. R. Mao, Z. Q. Yang, S. L. Wang, X. X. Wang, X. Hu, and R. M. Ma, A high-performance topological bulk laser based on band-inversion-induced reflection, Nat. Nanotechnol. **15**, 67 (2020).

[36] K. Liu, L. Shen, and S. He, One-way edge mode in a gyromagnetic photonic crystal slab, Opt. Lett. **37**, 4110 (2012).

[37] S. Raghu and F. D. M. Haldane, Analogs of quantum-Hall-effect edge states in photonic crystals, Phys. Rev. A **78**, 033834 (2008).

[38] F. D. M. Haldane and S. Raghu, Possible Realization of Directional Optical Waveguides in Photonic Crystals with Broken Time-Reversal Symmetry, Phys. Rev. Lett. **100**, 013904 (2008).

[39] Z. Wang, Y. D. Chong, J. D. Joannopoulos, and M. Soljačić, Reflection-Free One-Way edge Modes in a Gyromagnetic Photonic Crystal, Phys. Rev. Lett. **100**, 013905 (2008).

[40] Z. Wang, Y. Chong, J. D. Joannopoulos, and M. Soljačić, Observation of unidirectional backscattering-immune topological electromagnetic states, Nature (London) **461**, 772 (2009).

[41] X. Ao, Z. Lin, and C. T. Chan, One-way edge mode in a magneto-optical honeycomb photonic crystal, Phys. Rev. B **80**, 033105 (2009).

[42] J. X. Fu, R. J. Liu, and Z. Y. Li, Robust one-way modes in gyromagnetic photonic crystal waveguides with different interfaces, Appl. Phys. Lett. **97**, 041112 (2010).

[43] J. X. Fu, J. Lian, R. J. Liu, L. Gan, and Z. Y. Li, Unidirectional channel-drop filter by one-way gyromagnetic photonic crystal waveguides, Appl. Rev. Lett. **98**, 211104 (2011).

[44] Y. Poo, R. X. Wu, Z. Lin, Y. Yang, and C. T. Chan, Experimental Realization of Self-Guiding Unidirectional Electromagnetic Edge States, Phys. Rev. Lett. **106**, 093903 (2011).

[45] J. Lian, J. X. Fu, L. Gan, and Z. Y. Li, Robust and disorder-immune magnetically tunable one-way waveguides in a gyromagnetic photonic crystal, Phys. Rev. B **85**, 125108 (2012).

[46] G. G. Liu, P. Zhou, Y. Yang, H. Xue, X. Ren, X. Lin, H. X. Sun, L. Bi, Y. Chong, and B. Zhang, Observation of an unpaired photonic Dirac point, Nat. Commun. **11**, 1873 (2020).

[47] E. Colomés and M. Franz, Antichiral Edge States in a Modified Haldane Nanoribbon, Phys. Rev. Lett. **120**, 086603 (2018).

[48] D. Bhowmick and P. Sengupta, Anti-chiral edge states in Heisenberg ferromagnet on a honeycomb lattice, Phys. Rev. B **101**, 195133 (2020).

[49] S. Mandal, R. Ge, and T. C. H. Liew, Antichiral edge states in an exciton polariton strip, Phys. Rev. B **99**, 115423 (2019).

[50] J. F. Chen, W. Y. Liang, and Z. Y. Li, Revealing photonic Lorentz force as the microscopic origin of topological photonic states, Nanophotonics (2020), doi:10.1515/nanoph-2019-0428.

[51] W. Tong, J. Wang, J. Wang, Z. Liu, Y. Pang, and S. Qu, Magnetically tunable unidirectional waveguide based on magnetic photonic crystals, Appl. Phys. Lett. **109**, 053502 (2016).

[52] J. Shen, S. Liu, H. Zhang, S. T. Chui, Z. Lin, X. Fan, X. Kou, Q. Lu, and J. Q. Xiao, Robust and tunable one-way magnetic surface plasmon waveguide: an experimental demonstration, Plasmonics **7**, 287 (2012).